Morphology and Intramolecular Interactions in P(VDF-TrFE) Electrospun Nanofibers Doped with Disperse Orange 3 Dye: A Joint Infrared Spectroscopy and Electron Microscopy Study

Alessia Arrigoni, Gianluca Serra, Jacopo Manidi, Chiara Bertarelli, and Chiara Castiglioni*
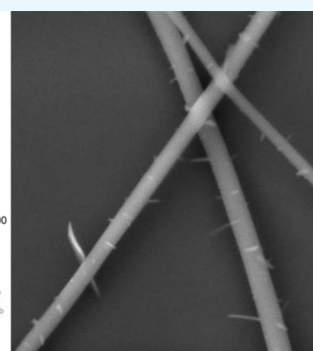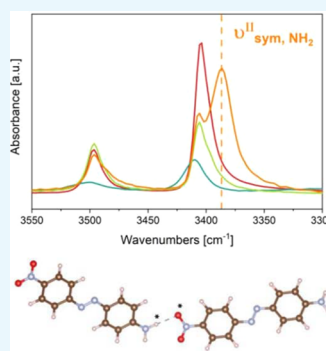
Read Online

ACCESS | Metrics & More | Article Recommendations | SI Supporting Information

ABSTRACT: In this study, we describe a host−guest system consisting of a push−pull dye, the 4-amino-4′-nitroazobenzene (Disperse Orange 3, **DO3**), mixed with the copolymer poly-(vinylidene fluoride-co-trifluoroethylene) [**P(VDF-TrFE)**] as a potential candidate for nonlinear optics (NLO) applications. We developed electrospun nanofibers of the polymer/dye blend, showing a highly anisotropic molecular structure, where **DO3** molecules are mostly oriented parallel to the polymer chain, running in the fiber axis direction. The technique opens a way for obtaining non-centrosymmetric ordering of the NLO chromo-phore without requiring further poling. The supramolecular architecture is deeply investigated through infrared vibrational spectroscopy, which allows detecting a new phase involving **DO3** molecules linked together by strong directional H-bonds. Electron microscopies highlight peculiar nanofiber morphologies with a preferred localization of **DO3** at the surface layers.

1. INTRODUCTION

Push−pull organic molecules are promising candidates for nonlinear optics (NLO) offering several advantages when compared to traditional inorganic materials such as $LiNbO_3$.[1−6] A key requirement to induce first-order nonlinear optical properties in a material is to prevent the formation of structures with inversion symmetry, both considering the supramolecular architecture and the intermolecular interactions.[5,6] Unfortunately, push−pull compounds often give rise to architectures with molecules arranged as closely packed dimers, forming pairs with antiparallel dipoles.[3,4] These geometries usually confer to crystal structures characterized by inversion symmetry; moreover, even in disordered (e.g., amorphous) matter, the NLO activity is completely lost because of the cancelation of β in the pairs and/or bulk isotropy.

Aggregation of the molecules into dimers can be hindered by embedding the active molecules in a polymeric matrix, forming a host−guest system. In this case, the macroscopic orientation of the active molecules is generally achieved by electric poling above the polymer glass transition temperature $T_g > T_{amb}$, and it is then frozen at ambient temperature.[6,7] In such systems, NLO performances such as second harmonic generation have been demonstrated.[8,9] Polymers containing NLO dyes are of great interest due to several advantages, such as: (i) they are cost-effective and easy to process; (ii) organic materials are easy to tailor to meet specific application requirements; and (iii) they are compatible with existing semiconductor technologies.[5−9]

Also, the specific design of the host polymer and the guest molecule and their possible combinations add a further degree of versatility.[9] Therefore, non-covalent supramolecular interac-tions play a key role in the design of host−guest polymeric materials with NLO activity. In fact, they influence the efficiency and the retaining of the long-term stability of the NLO response of the material by keeping the orientational order of the non-centrosymmetric organization of the dye.[6−8,10−14] Both interactions among polymer chains and those involving host−guest pairs can contribute to the stabilization of the final material architecture.[7,11] As guest molecules, azobenzenes with a push−pull character (i.e., π-conjugated azobenzene units bearing electron-donor and electron-acceptor substituents) are attrac-tive candidates.[7,8,10,12−15]

In this framework, we present a host−guest system where the push−pull azobenzene 4-amino-4′-nitroazobenzene (Disperse Orange 3, **DO3**) is blended with the copolymer poly(vinylidene fluoride-co-trifluoroethylene) **P(VDF-TrFE)**. The **DO3** dye exhibits a strong charge separation induced by its electron-withdrawing nitro group and electron-donor amino group, and it

has been recently proposed for NLO applications in blends with polymers.[7,10] In these works, infrared (IR) and Raman vibrational spectroscopies have allowed for a deep study of the relevant role of the intermolecular interactions between the **DO3** dye and the host polymer matrix.

Here, we deposit the **P(VDF-TrFE)/DO3** blend by electrospinning, where the high applied electric field drives the formation of nanofibers with both the polymer chains and the dye oriented in the as-spun material without the need of any post-processing poling to induce NLO chromophore ordering. We select the copolymer **P(VDF-TrFE)** as the host as fluorinated polymers and copolymers have been applied in many technological fields, including polymer optical fibers (POFs) and waveguides.[16−19] It is worth noting that **P(VDF-TrFE)** carries both electron-rich (fluorine) and electron-poor (hydrogen) atoms, which can give non-negligible electrostatic interactions with polar groups, thus allowing the formation of stable interacting polymer−**DO3** molecular complexes. We recently developed **P(VDF-TrFE)** electrospun nanofibers exhibiting high orientational order, with polymer chains well aligned with the fiber axis.[20] In the same work, we put together a set of tools for a thorough characterization of the polymer structure and morphology by means of vibrational spectroscopies, in conjunction with quantum chemical calculations.[20] This preceding study forms the basis for the development of the blend material and for its structural characterization.

In this paper, we show that both the electrospinning feed solution and the process parameters play a relevant role in generating peculiar fiber morphologies of the **P(VDF-TrFE)/DO3** blend. These morphologies are characterized by means of scanning electron microscopy (SEM) and transmission electron microscopy (TEM), showing that the fibers are characterized by a superficial cladding of the **DO3**-enriched material. We exploit IR spectroscopy to monitor changes in the molecular structure and intermolecular interactions while varying the relative dye/polymer concentration of the feed solution and the applied voltage. Moreover, IR analysis allows us to investigate the effect of subsequent treatments on the electrospun samples, for example, annealing and prolonged water rinsing. By means of quantum chemical simulations, we provide a coherent interpretation of the whole set of collected experimental data. Interestingly, we highlight the formation of a peculiar metastable phase of the blend, which is promoted by the electrospinning process and possibly related to effective molecular orientation phenomena.

2. RESULTS AND DISCUSSION

2.1. P(VDF-TrFE)/DO3 Blends: IR Spectra of Nanofibers and Films. IR spectra of the **P(VDF-TrFE)/DO3** blend processed as nanofibers and thin films show the spectral features of the copolymer together with several absorption peaks attributed to the **DO3** dye, see Figure 1a. In the region 1800−700 cm^{-1}, the spectral features of the copolymer in the blend do not show significant alterations in band shapes and peak frequencies with respect to the IR spectra of the electrospun neat copolymer (blue dashed spectra), except for the appearance of peaks related to the **DO3** dye (Figure 1b). In this region, most of the **DO3** peaks in the blend—highlighted by black lines in Figure 1b and listed in Table 1—find an excellent frequency match with the spectrum of the **DO3** powder. **DO3** peaks present in the powder spectrum but not highlighted in Figure 1b fall under the copolymer absorption bands, slightly modifying their shapes.
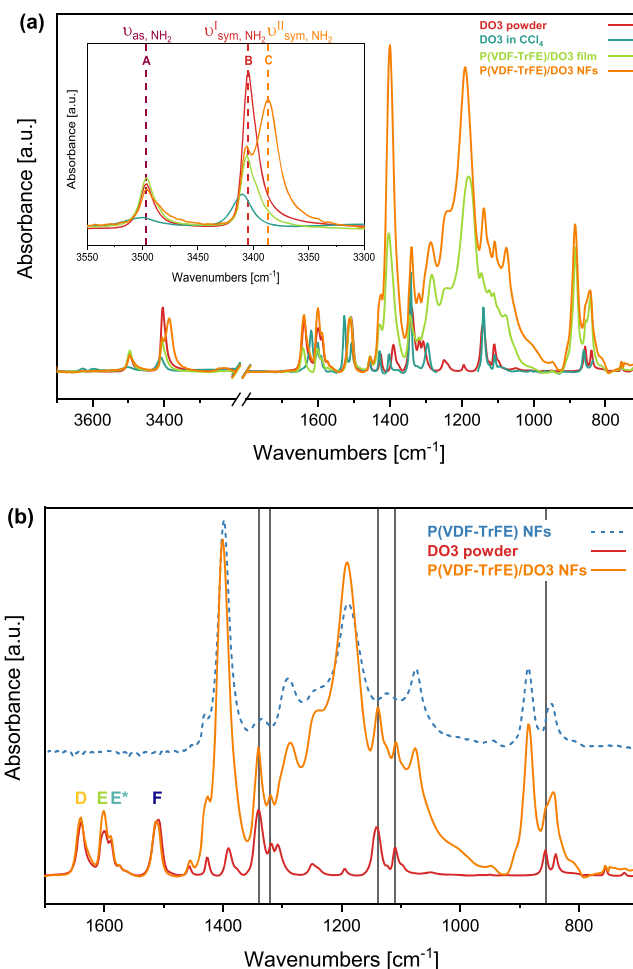

Figure 1. (a) Experimental IR spectra of **P(VDF-TrFE)/DO3** blends with 10% w/w **DO3** as nanofibers (orange) and films (green); experimental IR spectra of **DO3** in CCl$_4$ (blue) and crystal (red). Zoom inset: region of NH$_2$ stretching bands, showing major changes in different samples. Peak (A) NH$_2$ asymmetric stretching $\nu_{as,\ NH_2} \approx 3496$ cm^{-1}, peak (B) NH$_2$ symmetric stretching $\nu^I_{sym,\ NH_2} \approx 3405$ cm^{-1}, and peak (C) low-frequency NH$_2$ symmetric stretching $\nu^{II}_{sym,\ NH_2} \approx 3386$ cm^{-1}. (b) Experimental IR spectra of **P(VDF-TrFE)/DO3** blends with 10% w/w **DO3** as nanofibers (orange), of the **DO3** crystal (red), and **P(VDF-TrFE)** nanofibers (dashed blue spectra); straight lines indicate **DO3** spectral features that appear in the blend spectra in the copolymer region; D, E, E*, and F are bands of **DO3** occurring in a region free from absorptions of the copolymer (see Table 1 for the vibrational assignment). The absorbance scale of all spectra is normalized to the 1509 cm^{-1} peak.

Nevertheless, the spectral region around 3550−3300 cm^{-1}—where $\nu_{sym,\ NH_2}$ and $\nu_{as,\ NH_2}$ bands lie (see the zoom inset in Figure 1a)—shows some interesting phenomena. These NH$_2$ stretching vibrational modes are related only to **DO3**, and they show some remarkable variations in electrospun **P(VDF-TrFE)/DO3** samples with respect to the spin-coated film. These differences mainly involve the lower frequency transitions (bands around 3400 cm^{-1}), which are assigned to the NH$_2$ symmetric stretching $\nu_{sym,\ NH_2}$. In particular, the $\nu_{sym,\ NH_2}$ peak appears at the same frequency, namely, at 3405 cm^{-1}, for the **DO3** powder and the **P(VDF-TrFE)/DO3** spin-coated film (band B, Figure 1a), while for electrospun fibers, we clearly identify two distinct components. The higher frequency one,

Table 1. Band Assignment of DO3 Spectra in the Spectral Range Free from P(VDF-TrFE) IR Transitions (3700−1400 cm⁻¹), See Figure 1a; The Assignment Is Based on DFT Simulations (See Section 2.4)

exp wavenumbers [cm⁻¹]	label	polarization	vibrational assignment
3496	A	np	ν_{as} NH$_2$ anti-symm stretching
3405	B	//	ν^I_{sym} NH$_2$ symm stretching
3386	C	//	ν^{II}_{sym} NH$_2$ symm stretching
1639	D	//	CC stretching of the aniline unit + NH$_2$ bending + CN stretching
1600	E	//	CC stretchings of the nitrobenzene unit + NH$_2$ bending
1590	E*	//	CC stretchings of the nitrobenzene unit + NN stretching + anti-symm NO$_2$ stretching
1509	F	np	NO$_2$ anti-symm stretching + CC stretchings + NH$_2$ bending

with maximum at about 3405 cm⁻¹—band B in Figure 1a—coincides with the main absorption of the other samples, while a stronger, lower frequency component (band C) arises at 3386 cm⁻¹. Figure 1 shows the spectrum of a crystalline **DO3** powder. Although the crystal structure of **DO3** is still unknown, quantum chemical simulations suggest that it contains stacked **DO3** dimers, with antiparallel dipole moments.[7] **DO3** dissolved in CCl$_4$ presents a ν_{sym, NH_2} peak, showing just a small shift to higher wavenumbers with respect to the solid, see the zoom inset in Figure 1a. This observation suggests that, for neat **DO3**, the crystal packing only slightly affects the vibrational frequencies of

the -NH$_2$ group, thus supporting the hypothesis that intermolecular interactions mainly involve the π-electron system.

The new component identified for **P(VDF-TrFE)/DO3** nanofibers, namely, the peak C (hereafter referred to as ν^{II}_{sym, NH_2}), shows a noticeable wavenumber shift (of 20 cm⁻¹) with respect to the ν^I_{sym,NH_2}, B peak. The low wavenumber of the ν^{II}_{sym, NH_2} peak is related to **DO3** molecules in a peculiar phase and/or **P(VDF-TrFE)/DO3** interactions, both involving strong interactions of the NH$_2$ group, which are promoted by electrospinning.

It is worth noting that the anti-symmetric stretching band (ν_{as, NH_2}, peak A) is located at about the same position for all the samples analyzed, only showing a shoulder at the lower wavenumber side in the case of nanofibers.

2.2. Effects of the Process Parameters. *2.2.1. DO3 Concentration.* Polymer samples containing a different amount of dye show a very interesting behavior on the appearance of ν^{II}_{sym, NH_2} (see the IR spectra of **P(VDF-TrFE)/DO3** nanofibers and spin-coated films at different dye concentrations in Figure 2). The ν^{II}_{sym, NH_2} peak arises in the films at the lower **DO3** concentrations, whereas for nanofibers, the intensity of the ν^{II}_{sym, NH_2} peak increases with the increase of the concentration of the dye. In particular, the ν^{II}_{sym, NH_2} peak is absent at very low **DO3** concentration (2.5% w/w), where only the ν^I_{sym, NH_2} component is present. At a 5% w/w dye concentration, the ν_{sym, NH_2} band is split into two contributions, with the arising of
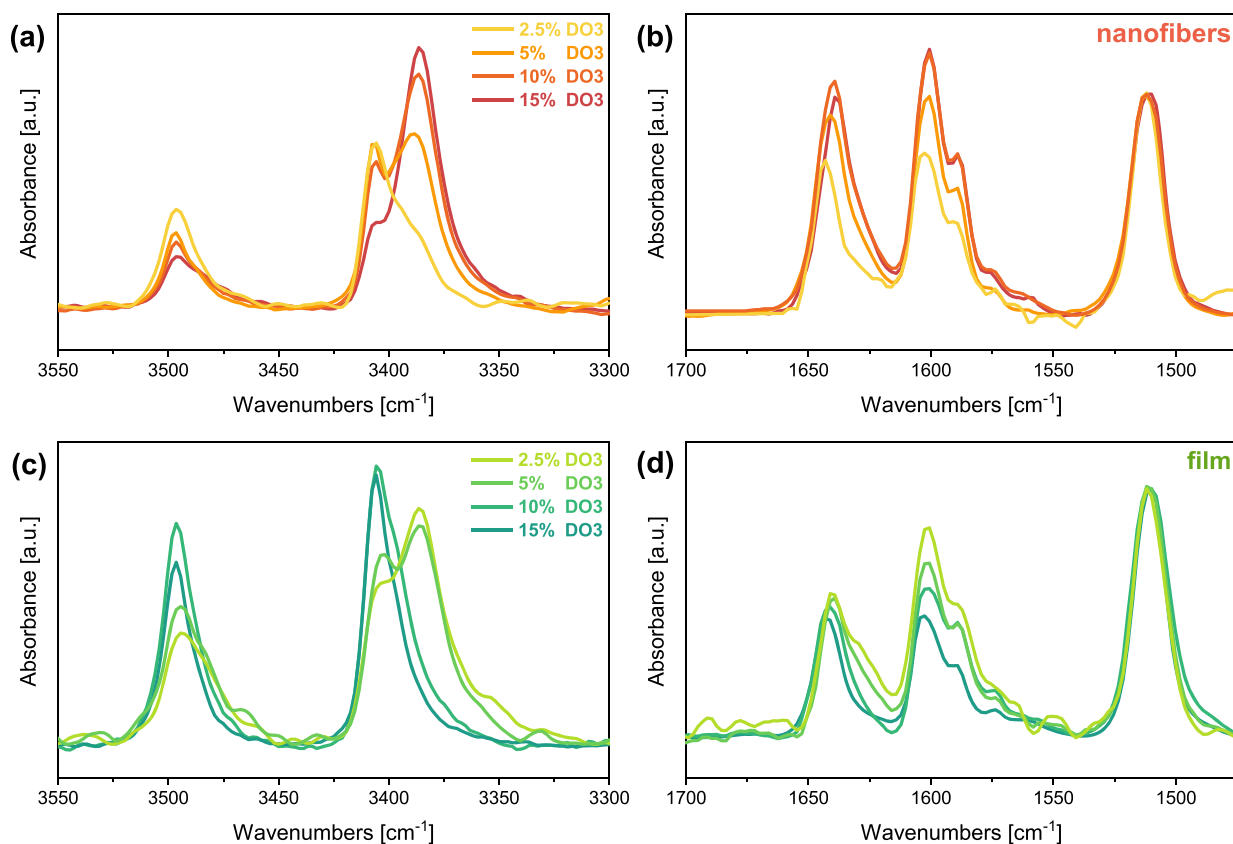

Figure 2. Experimental IR spectra of **P(VDF-TrFE)/DO3** blends at different dye concentrations. Samples are nanofibers (a, b) and films (c, d). The absorbance scale of all spectra is normalized to the 1509 cm⁻¹ peak.

the $\nu_{\text{sym, NH}_2}^{\text{II}}$ peak. By further increasing the concentration from 10 to 15% w/w, the intensity of the lower frequency $\nu_{\text{sym, NH}_2}^{\text{II}}$ peak increases with respect to the $\nu_{\text{sym, NH}_2}^{\text{I}}$ peak. Conversely, in the case of the films, the maximum intensity of the $\nu_{\text{sym, NH}_2}^{\text{II}}$ peak corresponds to the lowest dye concentration (2.5% w/w). By increasing the **DO3** concentration, this peak gradually disappears: at 10% w/w, it can be hardly detected as a weak shoulder of the main band, and at a 15% w/w concentration, only one sharp B peak $\nu_{\text{sym, NH}_2}^{\text{I}}$ is present (see Figure 2c).

Interestingly, nanofibers and thin films show an opposite trend with the increase of DO3 concentration, and the above observations suggest that two different phenomena, taking place in different concentration regimes, lead to the rise of the same (i.e., same wavenumber) $\nu_{\text{sym, NH}_2}^{\text{II}}$ peak in films and nanofibers.

The behavior of the spectra of **P(VDF-TrFE)/DO3** films at different dye concentrations has been already observed in an analogous spin-coated film of DO3 in PMMA in ref 7, with an increasing intensity of a low wavenumber band (corresponding to the $\nu_{\text{sym, NH}_2}^{\text{II}}$ band) while lowering the **DO3** concentration. The authors suggested that here the $\nu_{\text{sym, NH}_2}^{\text{II}}$ band is the marker of a specific polymer−dye interaction, characterized by hydrogen bond formation. These interactions take place only at very low **DO3** concentrations, namely, when $\pi−\pi$ interactions between **DO3** pairs are prevented. Conversely, in films prepared with high concentrations of **DO3**, the $\nu_{\text{sym, NH}_2}$ peak, located at the frequency characteristic of the crystalline phase of **DO3**, is compatible with **DO3** π-stacked dimers formed by the aggregation of the dye.[7]

Although the behavior of **P(VDF-TrFE)/DO3** films could be justified following ref 7, actually the above explanation cannot be applied in the case of the blend nanofibers analyzed here, since at the highest concentrations, they almost show only the $\nu_{\text{sym, NH}_2}^{\text{II}}$ peak. This suggests that the phenomena underlying the appearance of $\nu_{\text{sym, NH}_2}^{\text{II}}$ have a different origin related to the electrospinning process, which drives the appearance of a peculiar **P(VDF-TrFE)/DO3** phase highlighted by the marker band $\nu_{\text{sym, NH}_2}^{\text{II}}$.

Considering the electrospinning instability phenomena, we analyzed a set of 16 **P(VDF-TrFE)/DO3** electrospun samples with 10% w/w **DO3** to assess the reliability of the experimental data so far commented. For all the samples, we show the intensity ratios of several **DO3** peaks with respect to the band at 1509 cm^{-1} (F band), which is selected as a reference, since it is poorly sensitive, both in peak wavenumber and band shape, to the sample preparation condition (Figure 3). Regardless of some spreading of the data, the remarkable result is that the C band is always present and it is stronger than the B band in all samples. This definitely confirms that the phase associated with $\nu_{\text{sym, NH}_2}^{\text{II}}$ is predominant in all the electrospun mats.

2.2.2. Applied Voltage. Spin-coating and electrospinning are wet processing techniques, both characterized by fast solvent evaporation. However, in electrospinning, materials are also subjected to external forces driven by the strong applied electric field, where the polymer jet is stretched along the complex looped flight, while it shrinks due to solvent evaporation. It follows that macromolecular chains often tend to be preferentially oriented along the fiber axis, as well as small molecules dispersed into the feed solution.[33] Here, having a strong dipole moment, we expect that **DO3** effectively
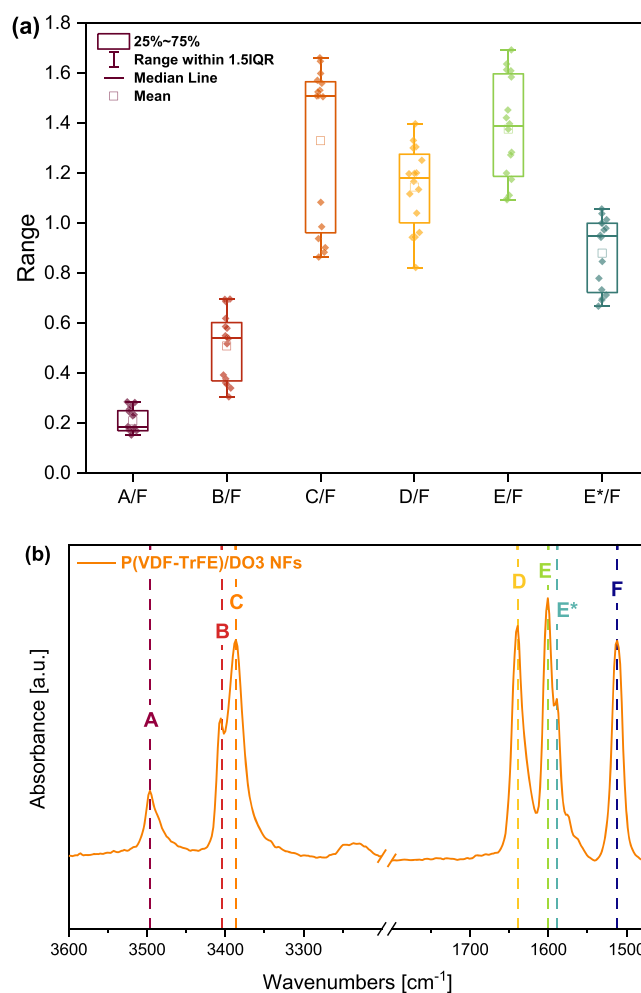

Figure 3. (a) Box plot of the intensity ratios of the peaks X with respect to the reference peak F. The intensity ratios (X/F) are obtained from peak heights after baseline correction. The analysis is carried out on the IR spectra of 16 **P(VDF-TrFE)/DO3** electrospun samples at the 10% w/w **DO3** concentration. Peak labels are defined according to (b), which show a representative IR spectrum, and Table 1.

experiences the electric field, inducing molecular orientation (see the discussion on molecular orientation, Section 2.5.1).

In order to investigate the effect of the applied voltage on the strength of the $\nu_{\text{sym, NH}_2}^{\text{II}}$ band, we decided to prepare samples at a low dye concentration (5% w/w) which presents a low intensity of the $\nu_{\text{sym, NH}_2}^{\text{II}}$ peak at the standard processing voltage (17 kV). The IR spectra of nanofibers deposited at increasing processing voltages (see Figure 4) show a remarkable dependence of the spectral pattern on the applied electric field. At lower voltages, the $\nu_{\text{sym, NH}_2}^{\text{II}}$ peak is rather weak, while at the higher voltages, a huge amount of the new phase gives rise to a very strong $\nu_{\text{sym, NH}_2}^{\text{II}}$ peak. Such evidence supports the hypothesis that the growth of the new phase is favored by the strong applied electric field the electrospinning is based on.

2.3. P(VDF-TrFE)/DO3 Fiber Morphology. *2.3.1. SEM Analysis.* SEM micrographs of **P(VDF-TrFE)/DO3** nanofibers show a peculiar morphology, with small branches emerging from the fiber surface (see Figures 5 and S5). These features have never been observed in our previous study on electrospun nanofibers of neat **P(VDF-TrFE)** at any process condition.[20] This implies that such a morphology is strictly related to the
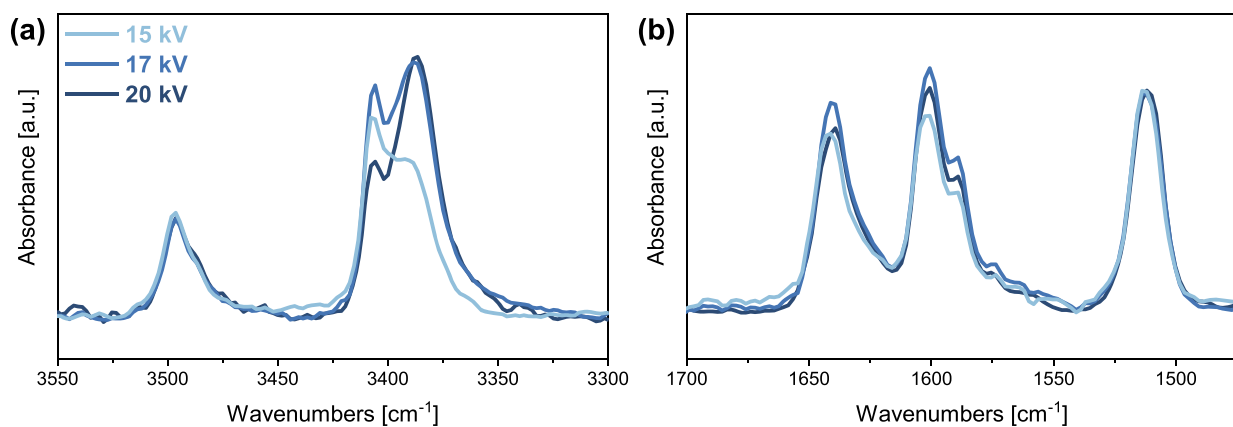
Figure 4. Experimental IR spectra of **P(VDF-TrFE)/DO3** nanofiber blends with 5% w/w **DO3**, processed at different operating voltages: (a) from 3550 to 3300 cm^{-1} and (b) from 1700 to 1450 cm^{-1}. The absorbance scale of all spectra is normalized to the 1509 cm^{-1} peak.
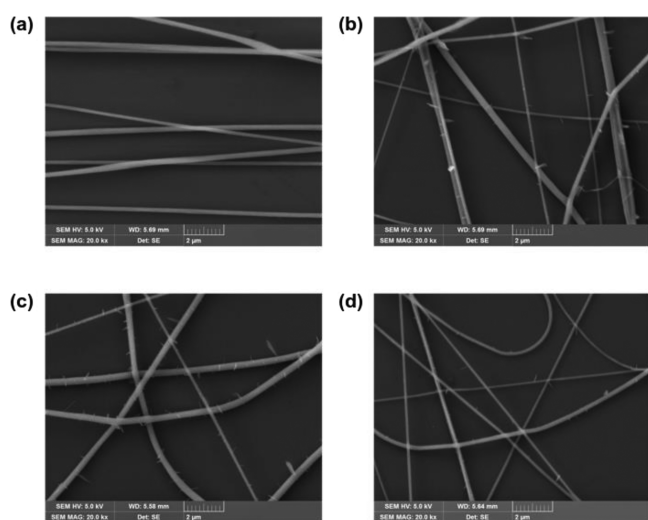

Figure 5. SEM micrographs of **P(VDF-TrFE)/DO3** nanofibers at different **DO3** concentrations, namely, (a) 2.5% w/w, (b) 5% w/w, (c) 10% w/w, and (d) 15% w/w. Diameter distributions are reported in SI from Figures S1 to S4.

presence of the dye. It is known that the formation of branched jets in electrospinning occurs because of local instabilities: the

simultaneous elongation of the flying jet and the rapid evaporation of the solvent can locally modify the charge per unit area carried by the jet.[34−36] The surface of the charged flying fluid jet can acquire a complex structure that becomes unstable at the sites of the highest local surface curvature.[34,37] To reduce the local charge accumulation, smaller secondary jets are formed from the main jet surface, creating branches. It is also noteworthy that the branched nanofibers obtained in this study have significantly smaller average diameters (around 200−300) than those deposited starting from a solution of **P(VDF-TrFE)** (around 600 nm), with the same electrospinning parameters.[20] This suggests that the high dielectric constant of **DO3** allows not only for a thinning of the spun fibers but also for an effective accumulation of charges on the flying jet, leading to branch formation.[35,38]

The amount of branches observed in SEM images at increasing **DO3** concentration (see Figure 5) nicely follows the trend of the ν^{II}_{sym, NH_2} peak intensity. Indeed, branches are almost absent for the fibers spun from solutions with the lowest dye concentrations (2.5% w/w), which show a rather weak ν^{II}_{sym, NH_2} band (Figure 2a). Instead, branches are more evident and thicker in the samples with higher dye concentrations (5, 10% w/w), showing a stronger ν^{II}_{sym, NH_2} IR peak. This suggests an existing correlation between the supramolecular structure/
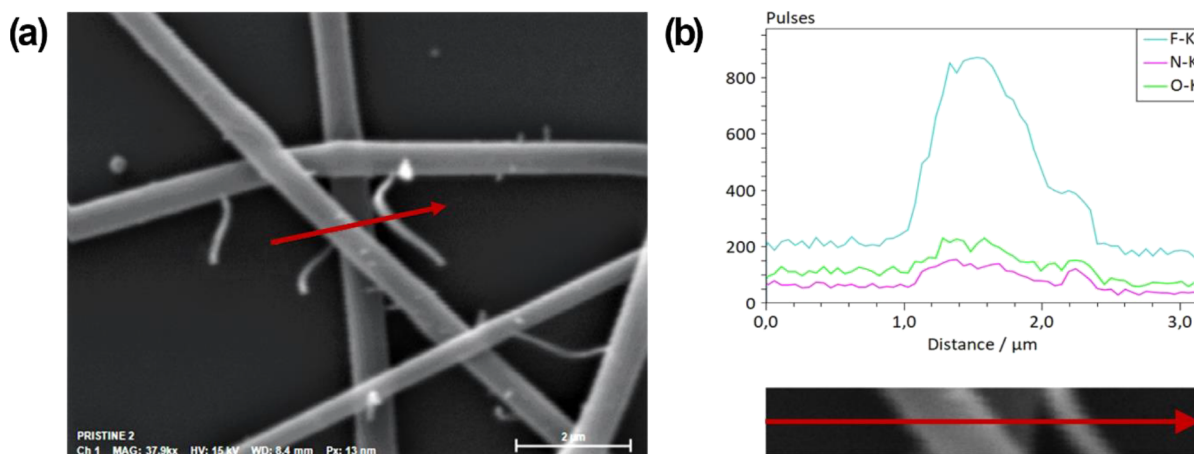

Figure 6. EDS line profile for the **P(VDF-TrFE)/DO3** nanofibers. (a) SEM image of the electrospun nanofibers. The arrow crosses the main fiber at about 1.6 μm and a thin branch at about 2.25 μm. (b) Elemental profile of F, N, and O atoms along the probed path.

intermolecular interactions of the **DO3** dye and electrospinning; moreover, it suggests that the thin branches are enriched in the new phase as it will be proven by the EDS analysis (see below).

2.3.2. Energy-Dispersive X-ray Spectroscopy. To complement SEM observations, EDS/SEM elemental analyses were carried out. From the line profile shown in Figure 6, it can be observed that the relative intensity of the **F** signal, which is characteristic of the polymer, compared to the **N** and **O** signals, is significantly more intense in the main fiber (at 1.60 μm) with respect to the secondary branch (at 2.25 μm). This means that the concentration of the dye in the mat is not constant, and **DO3** is more concentrated in the branches rather than in the fiber, suggesting that a partial **DO3** segregation on surfaces occurs.

2.3.3. TEM Analysis. TEM micrographs of nanofibers (see Figure 7) indicate the presence of a core-sheath structure, with a
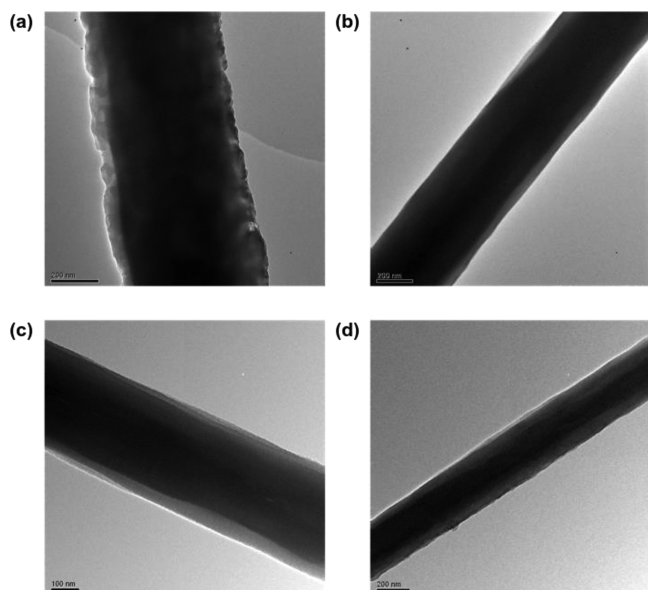

Figure 7. TEM micrographs of **P(VDF-TrFE)**/**DO3** nanofibers. (a, b) Nanofiber with 10% w/w **DO3**; c) nanofiber with 2.5% w/w **DO3**; (d) the same sample with 10% w/w **DO3** shown in (a, b) after thermal annealing at 90 °C.

porous and irregular surface outer layer. Branches are not detected by TEM, probably due to the damage of the extremely thin structures caused by the high acceleration voltage (200 kV). A similar core-sheath structure has been already reported for the nanofibers of PVDF blended with small molecules.[39,40] A brighter (less electron-dense) shell surrounds a darker (more electron-dense) region, suggesting that the polymer, which is rich in the fluorine atom, is more present in the core of the nanofibers, whereas a dye-rich phase is located at the outer region of the fiber.[39,40]

In our study, a brighter surface is clearly visible at any **DO3** concentration (see Figure 7a−c). To understand whether it is correlated with the abundance of **DO3** or specifically to the new **DO3** phase responsible of the ν^{II}_{sym, NH_2} peak, samples with a very low ν^{II}_{sym, NH_2} IR band intensity were also analyzed. In particular, we considered:

(i) **P(VDF-TrFE)**/**DO3** nanofibers with a very low concentration of the dye (2.5% w/w) (Figure 7c);

(ii) **P(VDF-TrFE)**/**DO3** (10% w/w) nanofibers subjected to thermal annealing up to 90 °C (Figure 7d), which also

show a drastic reduction of the new phase, according to IR measurements (see Section 2.5.2 for details).

In both the as-spun and in the annealed mats, TEM images show the core-sheath fiber morphology, not highlighting any evident morphological change.

This indicates that (i) the core-sheath structure is not specifically ascribed to the new **DO3** phase but to dye segregation phenomena, (ii) even at a low dye concentration, **DO3** undergoes segregation on the fiber surface, but the new **DO3** phase is not formed, and (iii) the structural rearrangements of the **DO3** supramolecular architecture occurring by annealing (see Section 2.5.2 and Figure 11) do not cause any evident modification of the fiber morphology.

2.4. Theoretical Models and Discussion. A shift to low vibrational frequencies of X−H stretching IR bands usually happens when a polar X−H bond is involved in a hydrogen bond (X−H...Y) with an acceptor atom Y belonging to another molecule or chemical group. This phenomenon can be ascribed to the weakening of the X−H bonds, as expected considering the limiting structure with a proton perfectly shared by the X and Y atoms.[41] Moreover, the H-bond formation is often accompanied by a raise of the X−H stretching intensity because of the increased electron charge mobility across the H bridge.[42] The above observations suggest to focus on H-bonded complexes possibly formed in the blend with the NH$_2$ group of **DO3** acting as the proton donor.

DO3 molecules could form H-bonds with electron-rich fluorine atoms of the CF$_2$ groups of the copolymer; therefore, the first suggestion is that the IR shift of the NH stretching band is due to guest **DO3** H-bonded to the host polymer matrix, as previously observed in the host−guest system with PMMA/DO3.[7]

To assign the NH stretching region of the observed IR spectra, DFT simulations have been applied to the following three classes of in vacuo molecular models:

(i) a **DO3** monomer (**M**);

(ii) two head-to-tail (HTT) dimers of **DO3** interacting through their NH$_2$ groups and already considered in the literature: one featuring a directional H...O interaction (**DH**) and the other with no directional interaction-(**D**).[7,10] These dimers correspond to the only two stable geometries we obtained for quasi-planar **DO3** HTT dimers at the level of theory selected;

(iii) two complexes containing a **DO3** monomer interacting through its NH$_2$ group with a PVDF oligomer with 10 repeating units, namely, CH$_3$(CF$_2$CH$_2$)$_{10}$CF$_3$ (**DP1** and **DP2**).

These five models are sketched in Figure 8.

Concerning **DP1** and **DP2**, an empirical force field (MMFF94) was used to determine the most stable structures starting from an initial set of guess conformations (see the Supporting Information for details). Theoretical IR spectra have been plotted as sums of Lorentzian functions. A full width at half-maximum of 10 cm^{-1} has been chosen in accordance with the experimental data.

2.4.1. DO3 Dimers. Inspired by previous studies concerning **DO3** dimers (see refs 7, 10), we consider HTT **DO3** systems within the level of theory adopted for the study of the large molecular complexes mimicking **DO3**...PVDF interactions.

The isolated monomer of **DO3** and its two HTT dimers, namely, structures **M**, **DH**, and **D**, are represented in Figure 8a−c, with asterisks marking the closest neighbor atoms involved in
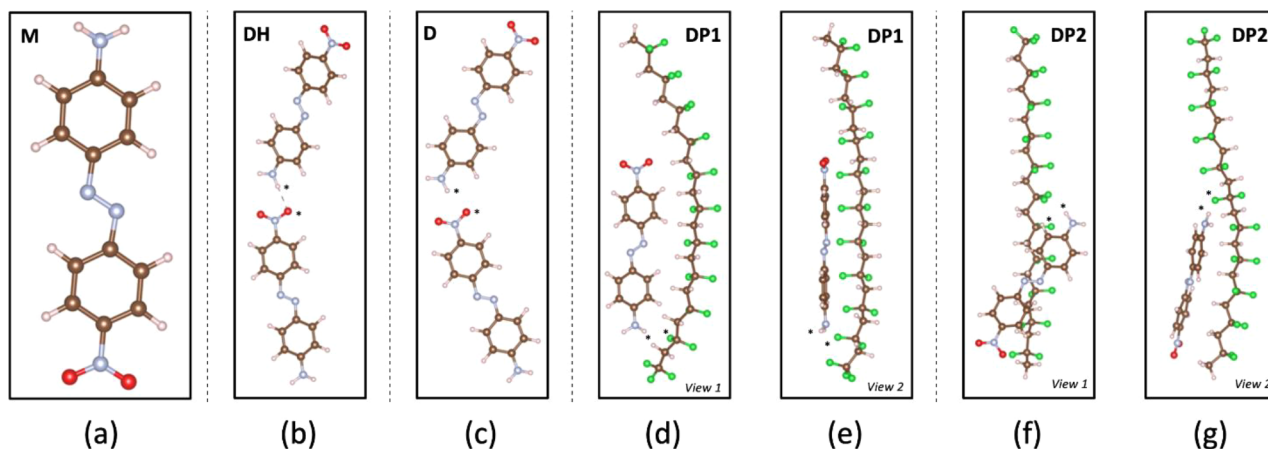
Figure 8. DFT equilibrium geometries of the in vacuo molecular models considered in this study (carbon is indicated in brown, hydrogen in white, nitrogen in light blue, fluorine in green, oxygen in red): the **DO3** monomer (indicated as **M**, (a)); an HTT dimer of **DO3** with a directional hydrogen interaction (**DH**, (b)); an HTT dimer of **DO3** with no directional interaction (**D**, (c)); two views of complexes of the **DO3** monomer and a $CH_3(CF_2CH_2)_{10}CF_3$, mimicking a PVDF sequence of the **P(VDF-TrFE)** copolymer (**DP1**, (d, e)); two views of another possible interacting system with **DO3** and PVDF (**DP2**, (f, g)). Asterisks mark the closest neighbor atoms involved in the interaction (geometrical parameters described in Table 2).

the interaction. As reported in Table 2, the two dimers **D** and **DH** have similar energies and **DO3...DO3** interaction results in

Table 2. DFT Equilibrium Properties of the Molecular Models, Where r_W Is a van der Waals Radius[a]

model	N−H bond length [Å]	H...O distance [Å]	r_W(H) + r_W(O) [Å]	N−H...O angle [°]	DFT relative energy per molecule [kcal/mol]
M	1.009				5.07
DH	1.012	2.055	2.72	179.6	0.00
D	1.010	2.156	2.72	164.1	0.01

model	N−H bond length [Å]	H...F distance [Å]	r_W(H) + r_W(F) [Å]	N−H...F angle [°]	DFT relative energy [kcal/mol]
DP1	1.010	2.102	2.67	140.2	0.00
DP2	1.011	2.165	2.67	158.2	7.68

[a]When meaningful, the first two columns refer to the interacting chemical groups defined in Figure 8; in both parts of the table, the DFT relative energies of the most stable systems (**DH** and **DP1**) have been arbitrarily set to zero.

a stabilization of the system, as well as in small variations of the N−H and N−O bond lengths. Moreover, the comparison of the length of the H...O intermolecular bond with the van der Waals radii of H and O atoms suggests that both the **DO3** dimers interact not only by dispersion forces but also through electrostatic forces. However, besides the shorter H...O distance in the **DH** complex, the most remarkable difference between the two dimers is the N−H...O angle, which determines an almost perfect alignment of the three atoms only in the case of **DH**, which is typical of strong, directional hydrogen bonds. Interestingly, even if the initial guess geometry for **DH** was a quasi-planar structure, after geometry optimization, the **DH** dimer exhibits a remarkably distorted structure, with phenyl rings of the two **DO3** partners lying on different planes.

Concerning the dimer **D**, we can infer that its structure is stabilized by an effective electrostatic interaction of the H* atom with both oxygen atoms of the NO$_2$ group: the distances between H* and the two oxygen atoms are indeed close in dimer **D**, with intermolecular bond lengths r(H*...O*) = 2.156 Å and r(H*...O) = 2.374 Å. A comparable stabilization energy of **DH** comes by the stronger, directional bond of H* with O* and a less
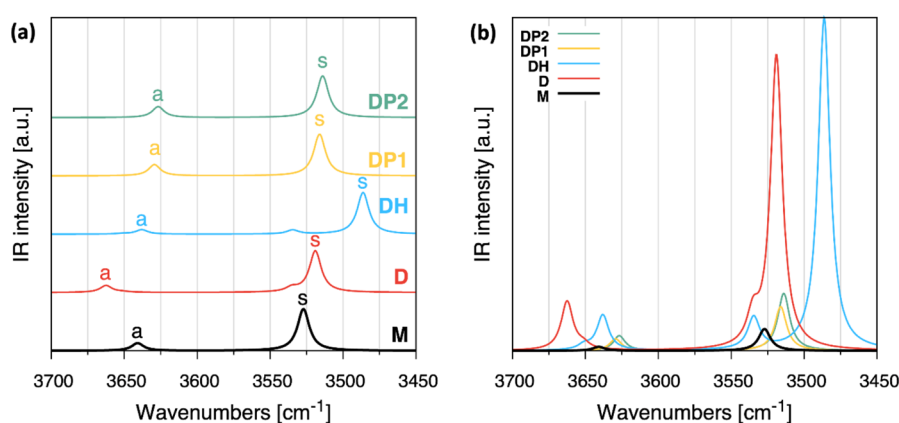

Figure 9. DFT IR spectra in the NH stretching wavenumber region. (a) Spectra normalized to unity and vertically translated as a matter of clarity, with the "s" and "a" labels marking the peaks assigned to symmetric and anti-symmetric NH$_2$ stretching modes localized in the interacting region defined in Figure 8. (b) The same spectra as in (a) are compared without normalization of the computed IR intensities.

effective electrostatic interaction with the second, more distant oxygen atom, with $r(\text{H*}...\text{O}) = 2.506$ Å. Interestingly, the two equilibrium geometries of the **DO3** dimers correspond to the only two minima of the potential energy surface of $(\text{DO3})_2$ HTT structures, while—at the level of theory adopted—a more symmetric "chelated" geometry, where each H atom of the NH_2 group forms non-directional H bonds with a different atom of NO_2, results to be not stable. This finding is in partial disagreement with the results reported in ref 10. In that work, besides a H-bonded dimer showing a structure very similar to **DH**, a second, quasi-chelated **DO3** dimer is identified as further equilibrium structures of $(\text{DO3})_2$, showing an HTT configuration.

Based on this fact and noticing the similar energies of **D** and **DH** as well as the existence of stable non-HTT **DO3** dimers,[7] we realize that the potential energy landscape around a **DO3** molecule is rather complex, and its description is very sensitive to the theoretical method adopted. Moreover, simply considering the peculiar chemical structure of **DO3**, we can infer that many minimum-energy conformations are available for supramolecular complexes involving **DO3**. Indeed, **DO3** exhibits a large dipole moment, and it shows electron-rich regions near the N═N bond and NO_2 group, together with electron-poor hydrogen atoms of the NH_2 group. Moreover, delocalized π electrons of the phenyl rings and a quasi-flat molecular backbone can stabilize supramolecular architectures through effective $\pi-\pi$ stacking.

The DFT-simulated IR spectra of **M**, **D**, and **DH** are reported in Figure 9. The IR band of **DH**, related to the symmetric NH stretching, indicated with "s", is substantially red-shifted with respect to **M**. We identify this as the main spectroscopic marker of directional hydrogen bond in **DO3** dimers. In addition, Table 3 lists the values of the ratio I_s/I_a between IR intensities related

Table 3. DFT-Computed Frequencies and IR Intensities of Symmetric and Anti-Symmetric NH Stretching Vibrational Normal Modes[a]

model	I_s	I_a	I_s/I_a	ν_s	ν_a
DP2	323.50	84.49	3.83	3514	3627
DP1	248.60	67.04	3.71	3515	3629
DH	1876.00	198.90	9.43	3486	3638
D	1657.00	275.60	6.01	3519	3662
M	122.60	22.33	5.49	3527	3641

[a]IR intensities are labeled with I and given in units of km/mol; scaled frequencies are indicated with ν and given in units of cm^{-1}; subscripts "a" and "s" Refer to the anti-symmetric and symmetric NH stretching modes, respectively.

to symmetric and anti-symmetric NH stretching vibrational modes. We observe that the formation of **DH** also results in a non-negligible increase of I_s/I_a, which consequently provides another spectroscopic marker of directional hydrogen bond interaction in **DO3** dimers.

To summarize, **D** and **DH** are both equally stable with respect to **M**, but the directionality of the interaction featured by **DH** results in a strong frequency shift and IR intensity increase of the band related to symmetric NH stretching.

2.4.2. DO3—PVDF Clusters.
We now focus on models **DP1** and **DP2**, where a monomer of **DO3** interacts with an oligomer of PVDF (see Figure 8d−g). This should mimic the interaction between a **P(VDF-TrFE)** and **DO3** molecules, occurring in the blend.

Looking again at Table 2, we see that both **DP1** and **DP2** are characterized by strong electrostatic intermolecular interactions that are not directional hydrogen bonds due to the absence of nuclear alignment. The absence of H-bond directionality reflects in the IR spectra shown in Figure 9, where only a minor red shift with reference to **M** results for the symmetric NH stretching band. Moreover, the frequency of this band is very close to that of the **D** model (see Table 3). This means that the NH stretching region of the IR spectrum is quite insensitive with respect to the formation of **DO3-PVDF** complexes.

Figure 9 and Table 3 also show a significant blue shift for the IR band related to the NH anti-symmetric stretching in the **D** model: this property is peculiar of **D**, and it can be considered its spectroscopic marker. This feature, however, seems to be completely absent in the experimental spectra of **DO3** blends: we thus conclude that our samples do not contain HTT **D** dimers with no directional interactions, or they are present only in a small amount.

We thus conclude that

(i) the red shift of the IR band of **DH** is related to the symmetric NH stretching involving a H-bond which forms a directional NH...O bridge;

(ii) the increase of relative IR intensity of the symmetric NH stretching band with respect to the one associated with anti-symmetric NH stretching is also a spectroscopic marker for the directional hydrogen interaction between **DO3** monomers.

According to the above results from DFT predictions, the peak $\nu_{\text{sym, NH}_2}^{\text{II}}$ observed in the experimental IR spectra of **P(VDF-TrFE)**/**DO3** blends is ascribed to the occurrence of strong directional H-bonds involving the NH_2 group of **DO3**.

In other words, our modeling suggests that **DO3** dimers (or possibly oligomers) can exhibit such a low $\nu_{\text{sym, NH}_2}^{\text{II}}$ wavenumber, only if they adopt a local conformation as that of the **DH** model. Accordingly, a chelated dimer (not found among the stable structures at the level of theory here adopted but proposed in ref 10.) as the stable HTT structure is expected not to show a significant red shift of the symmetric NH stretching band because directional H bonds are incompatible with a cyclic $NH_2....NO_2$ arrangement.

Moreover, our modeling of complexes shows that NH_2 units could be involved in electrostatic interactions with fluorine atoms belonging to PVDF units, but, also in this case, without the formation of any directional hydrogen bonds.

In conclusion, the observed occurrence of $\nu_{\text{sym, NH}_2}^{\text{II}}$ is due to the presence of HTT **DO3** dimers—or oligomers—with a structure like the **DH** model, and it is associated with a peculiar phase that, indeed, is abundant in nanofibers collected from solutions at high **DO3** content.

Its formation is likely related to the effective alignment of **DO3** molecules caused by the applied electric field during electrospinning, which promotes the formation of hydrogen-bonded dimers. Because of the rapid solidification, the preferential orientation and the HTT configuration of **DH** dimers could be almost quenched, thus preventing the formation of stacked dimers with an antiparallel orientation of the molecules.

The experimental evidence of the remarkable orientation of the **DO3** dye by the effect of the electric field and the proof that the freezing of the H-bonded phase is related to the rapid solvent evaporation of the electrospun jet are discussed in Section 2.5.
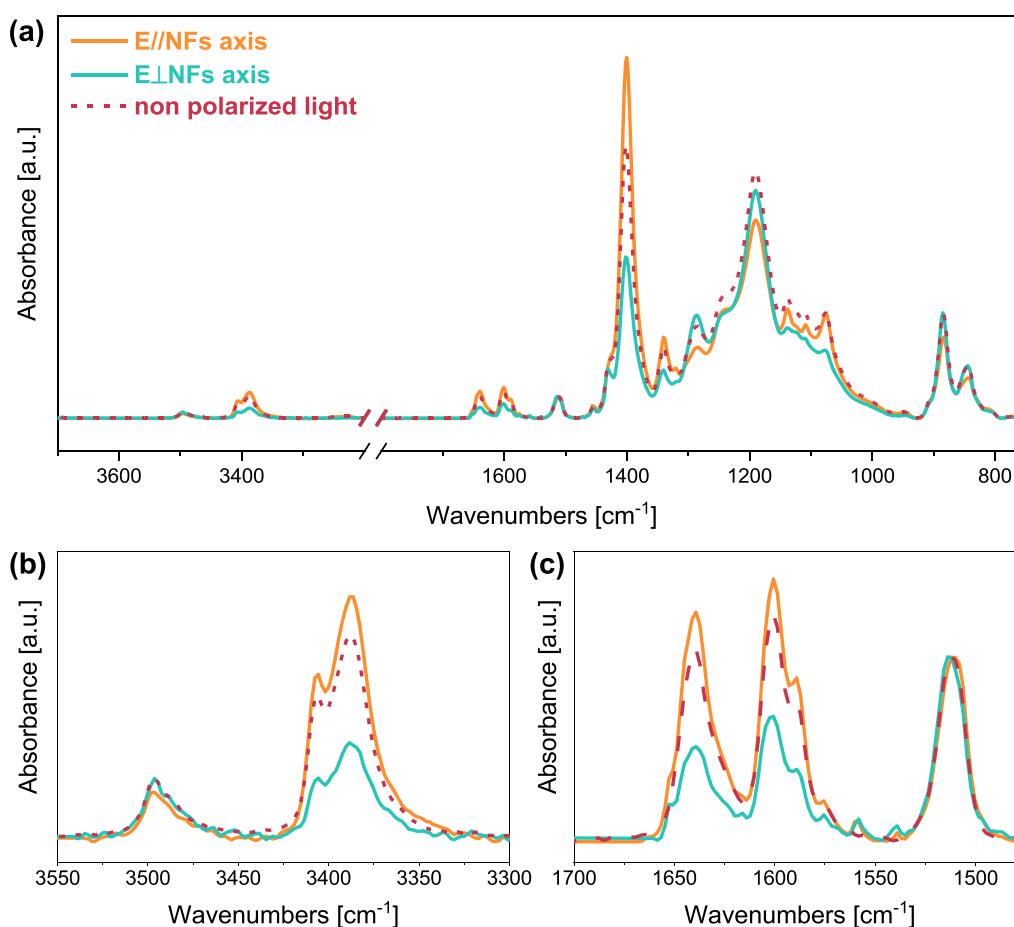
Figure 10. Experimental IR spectra of **P(VDF-TrFE)/DO3** nanofiber blends with a macroscopic orientation of the fiber axes. Spectra are recorded in polarized light in the direction parallel (orange line) and perpendicular (green line) to the fiber axis. The dashed spectrum is recorded in non-polarized light. (a) shows the whole spectra, while (b, c) highlights regions peculiar of the **DO3** molecule, from 3550 to 3300 cm^{-1} and from 1700 to 1450 cm^{-1}, respectively. The absorbance scale of all spectra is normalized to the 1509 cm^{-1} peak.

Moreover, the previously observed segregation phenomena (Section 2.3) suggest that regions rich in **DO3** develop, possibly forming an extended network involving **DO3** molecules linked together by strong H-bonds.

It is noteworthy that the ν^{I}_{sym, NH_2} peak at 3405 cm^{-1} does not completely disappear also for highly **DO3** concentrated nanofibers (Section 2.2.1), indicating that the dyes not forming **DH** dimers are also present in nanofiber samples. Unfortunately, the analysis of the NH$_2$ stretching region cannot help in recognizing possible complexes different from **DH** because the vibrational frequencies result to be rather insensitive to non-directional electrostatic interactions as those occurring in dimer **D** and in complexes with the polymer. Moreover, according to ref 7., π-stacked dimers do not exhibit appreciable frequency shifts, as experimentally proven by the fact that **DO3** powders show frequencies close to those of **DO3** in solution, as shown in Figure 1a.

2.5. Molecular Orientation and Fibers Post-Processing. *2.5.1. Macroscopically Oriented Fibers.* The molecular orientation can be investigated through polarized IR spectra of nanofibrous mats with a macroscopic alignment of the nanofibers (Figure 10). According to our previous study on **P(VDF-TrFE)** nanofibers,[20] some IR peaks of the copolymer in **P(VDF-TrFE)/DO3** nanofibers show dichroism, as expected: in particular, the high intensity shown by the band at about 1402 cm^{-1} in parallel polarization proves that polymer chains are mainly aligned along the main fiber axis.[1] Nevertheless, also **DO3** IR peaks show strong dichroism (see Figure 10b,c). In particular, the ν_{sym, NH_2} and the peaks related to the NH bending—CC stretching at 1640 cm^{-1} and around 1600 cm^{-1} show an increase in intensity when the sample is irradiated with light linearly polarized in the direction of the nanofiber axis. The behavior of the NH$_2$ stretching mode can be easily explained considering that it is a localized vibration, with the associated dipole moment vector oscillation roughly parallel to the long molecular axis of **DO3**. As the long axis of **DO3** almost coincides with the direction of the equilibrium molecular dipole, the molecules should orient in the field direction when subjected to the electric field during electrospinning. This results in the alignment of the **DO3** major axis in the same direction of polymer chains, that is, all parallel to the fiber axis. In this case, the dipole oscillation associated with the NH$_2$ symmetric stretching mode results to be directed along the fiber axis, and the associated band has parallel polarization.

Additionally, it is interesting to note that in non-polarized IR spectra of non-aligned fiber mats, the high intensity shown by ν^{II}_{sym, NH_2} comes from two different contributions:

(i) an increase in intensity is due to the fact that the molecules are aligned to the fiber axis, thus resulting in a dipole derivative vector parallel to the substrate plane;
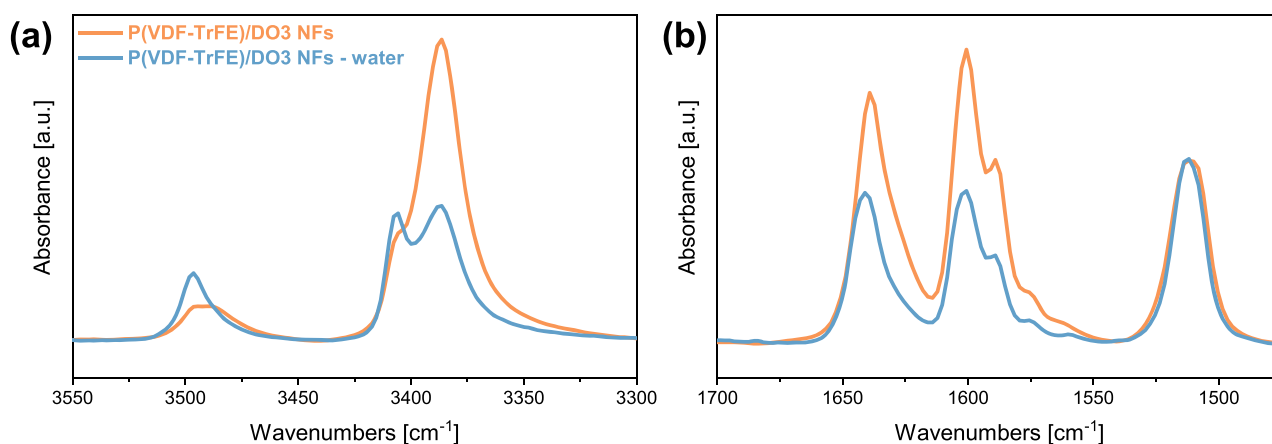
(1) Thermal annealing
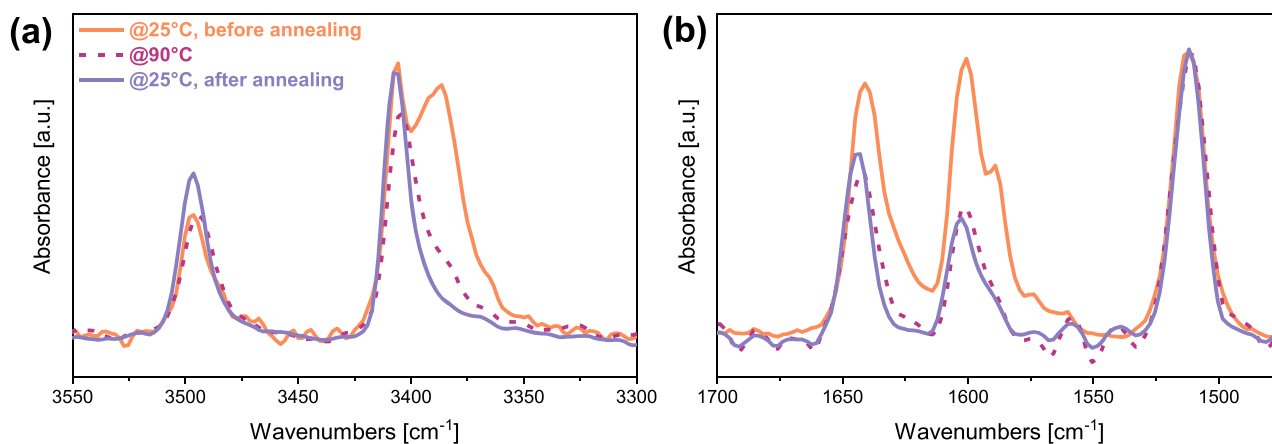
(2) Water rinsing

Figure 11. (1.a, b) Experimental IR spectra of **P(VDF-TrFE)**/**DO3** nanofibers with 5% w/w **DO3** before, during, and after thermal annealing. (2.a, b) Experimental IR spectra of the **P(VDF-TrFE)**/**DO3** nanofiber with 10% w/w **DO3** as spun (orange line) and after immersion in distilled water for 1 week (light blue line). The absorbance scale of all spectra is normalized to the 1509 cm^{-1} peak.

(ii) the directional H-bond itself produces a remarkable enhancement of the intrinsic intensity of the NH$_2$ symmetric stretching, as inferred through DFT modeling of the **DH** dimer.

These two effects are strongly interconnected since they both come from the electrospinning process, which induces the **DO3** molecular alignment and favors the formation of the here discussed new **DO3** phase with directional H-bonds. In addition, this metastable supramolecular architecture is stabilized by the fast solidification of the flying polymer jet.

2.5.2. Fiber Annealing and Water Rinsing. The H-bonded electrospinning-induced phase of **DO3** is a metastable condition. Figure 11 (1) shows the IR spectra of nanofibers with 5% w/w **DO3** heated up to the Curie temperature of the copolymer (about 130 °C) and then cooled down to room temperature. In the as-spun samples, the ν_{sym, NH_2} band is split into two peaks with almost the same height, in agreement with what was observed in Section 2.2.1. However, during the annealing, a transition is observed. In fact, at 90 °C, the ν_{sym, NH_2}^{II} band completely disappears (dashed spectra in Figure 11 (1)). Moreover, when the sample is cooled down to room temperature, the only contribution to the symmetric NH

stretching region is ν_{sym, NH_2}^{I}, without any recovery of the phase with ν_{sym, NH_2}^{II}. Similarly, in the region between 1600 and 1640 cm^{-1}, a weakening of the **DO3** features is observed upon annealing, which should be related to a different intrinsic intensity of these bands after the structural rearrangement of **DO3**. This interpretation is corroborated by the comparison of the IR spectra of the neat **DO3** in the solid state with the spectra of the blends in the form of films and of nanofibers, as shown in Figure 12. In the powder and in the film, the two bands (bands D and E, see Table 1 for peak labels) are always weaker with respect to the nanofibrous mat. The observed behavior indicates that the presence of directional H-bonding between **DO3** molecules in nanofibers (phase characterized by ν_{sym, NH_2}^{II}) leads to an increase of the intensity of bands D and E. Thus, the weakening of these two peaks observed after annealing can be taken as further evidence of the disappearance of the **DO3** H-bonded phase in nanofibers in favor of a supramolecular structure more similar to the one observed in crystalline powders.

Interestingly, despite the evident structural rearrangement of the blend at the molecular level, TEM images indicate that the core-sheath structure, observed before the annealing, is
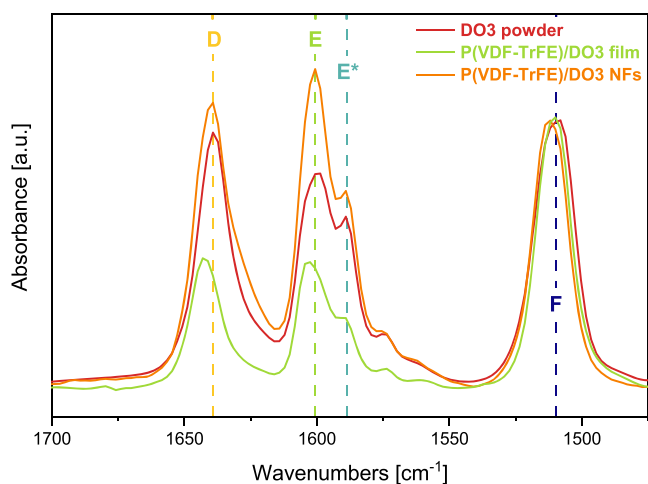
Figure 12. Experimental IR spectra in the region 1700−1400 cm^{-1} of **P(VDF-TrFE)/DO3** blends with 10% w/w **DO3** as nanofibers (orange) and film (green); experimental IR spectra of the **DO3** crystal (red). The absorbance scale of all spectra is normalized to the 1509 cm^{-1} peak.

preserved after the thermal treatment (see Section 2.3.3). The collection of the experimental findings allows to conclude that the thermal energy modifies the architecture of the superficial phase, enriched in **DO3**, in the annealed sample. In the outermost layers, **DO3** molecules lose their directional H bonds and relax into a more stable supramolecular arrangement, still maintaining their concentration profile with an enriched **DO3** concentration on the superficial layers. Since the annealing determines a change of the **DO3** supramolecular structure (disappearance of H-bonded dimers), we cannot exclude variation of the average fiber diameter.

Such a local rearrangement does not likely cause a meaningful reduction of the orientation order typical of chains and dye molecules in the fibers.

In addition, upon immersion of the nanofibrous mat in distilled water (for 1 week), almost no loss of material is evidenced. However, an important structural rearrangement is shown by the evolution of the **P(VDF-TrFE)/DO3** IR spectrum (Figure 11 (2)), where a remarkable weakening of the $\nu^{II}_{sym, NH2}$ peak is observed. The soaked sample has a high concentration of **DO3** (10% w/w), that is, it shows a noticeable initial contribution of the $\nu^{II}_{sym, NH2}$ peak. Nonetheless, a remarkable depletion of the $\nu^{II}_{sym, NH2}$ band intensity and an increase of the $\nu^{I}_{sym, NH2}$ peak follow the immersion in water. The dye is not dissolved by water, as proven by the fact that the intensity ratio (R) between the 1509 cm^{-1} band of **DO3** and of a polymer band (883 cm^{-1} peak) is almost not affected. The intensity ratio is $R = 0.311$ before water immersion and $R = 0.323$ after the treatment. Therefore, **DO3** undergoes a structural rearrangement when nanofibers are in contact with water, probably due to swelling with water molecules acting as plasticizers, thus leading to a more stable supramolecular architecture. Although the NH$_2$ symmetric stretching region shows the most evident variations, also NH$_2$ bending−CC stretching bands in the region of 1600−1640 cm^{-1} show a decrease in intensity after water immersion, as observed by annealing. These intensity variations further suggest a structural relaxation of the dye environment.

Interestingly, SEM images of the **P(VDF-TrFE)/DO3** nanofibers show the disappearance of branches after water

immersion (see SI, Figure S6). Since we have evidence that branches are not dissolved by water, they likely undergo a morphology rearrangement, favored by the high surface to volume ratio. This phase rearrangement is significant if we consider that the amount of the peculiar H-bonded **DO3** phase is very abundant in the branches, as previously discussed from IR spectroscopy and SEM/EDS analysis (see Section 2.3).

3. CONCLUSIONS

In this study, we deeply analyzed the supramolecular organization of dye molecules of interest for second-order NLO (**DO3**) embedded in a fluorinated polymer. The blended material is processed by electrospinning, resulting in core-sheath nanofibers with a preferential segregation of the dye at the fiber surface. Depending on the concentration of the dye in the polymer fiber, a peculiar phase involving **DO3** molecules linked by a strong directional H bond through their donor (NH$_2$) and acceptor (NO$_2$) groups is formed, resulting in

(a) the appearance of a new low-frequency IR peak for the NH$_2$ symmetric stretching vibrational mode, namely, ν^{II}_{sym, NH_2}, at 3386 cm^{-1};

(b) a significant intensity enhancement of the NH$_2$ stretching region because of the high intensity of the ν^{II}_{sym, NH_2} band.

Specifically, this peculiar **DO3** phase:

(i) is predominant at **DO3** concentration ≥ 10% w/w;

(ii) is strongly related and influenced by the voltage applied during electrospinning.

The assignment of the low-frequency ν^{II}_{sym, NH_2} band to **DO3** in the peculiar H-bonded arrangement is supported by quantum chemical calculations. The calculations revealed that only when an NH bond belonging to an NH$_2$ group is involved in a strong directional hydrogen bond with an oxygen atom of the **DO3** partner, a red shift of the symmetric NH$_2$ stretching occurs, together with a remarkable increase of its IR intensity. Interestingly, the observed intensity enhancement (point (b) above) of the band ν^{II}_{sym, NH_2} is a marker of the formation of directional H-bonds in the **DO3** phase, and it is also related to orientation phenomena. The remarkable anisotropy demonstrated by IR spectra in polarized light shows that the long axis of the **DO3** dye is aligned to the fiber axis. Being peculiar of the **P(VDF-TrFE)/DO3** nanofiber, this phase is a consequence of the strong electric field experienced by **DO3** molecules during electrospinning.

Furthermore, SEM images of **P(VDF-TrFE)/DO3** nanofibers show thin lateral branches which EDS analysis proved to be rich in **DO3**, thus indicating preferential segregation of **DO3**. TEM analysis clearly demonstrates a core-sheath structure of the fiber, with **DO3** phase segregation onto the outer region at any dye concentration, independently of the dye content and of the formation of the peculiar H-bonded **DO3** phase. Interestingly, the new phase undergoes a rearrangement upon thermal annealing or water rinsing without any loss of material and/or modifications in the fiber morphology.

In conclusion, we demonstrate that electrospinning **P(VDF-TrFE)** with an appropriate **DO3** concentration is effective for the formation of a segregated metastable phase of the dye in an outer fiber sheath. This sheath consists of **DO3** HTT structures highly oriented along the fiber axis and characterized by a strong and directional H-bond. The peculiar arrangement of the dye in the 10% w/w **DO3** core-sheath fibers allows the intrinsic

nonlinear optical properties of the push—pull azobenzene molecule to be retained in the final material, without requiring any post-processing poling.

4. EXPERIMENTAL AND THEORETICAL METHODS

4.1. Materials. *4.1.1. Solution Preparation.* All the materials were purchased from Sigma Aldrich and used without further purification, specifically Solvene 200/P400, namely, **P(VDF-TrFE)** (80/20) (M_w = 400,000 g mol^{-1}), **DO3** (90% dye content), *N,N*-dimethylformamide (DMF, 99.8%), and acetone (99.9%). The polymer was dissolved in a (4:6) volume ratio of DMF/acetone at a polymer/solvent concentration of 20% w/v. The solution was stirred at room temperature for about 1 h until a uniform and clear solution was obtained. For the preparation of host—guest polymeric samples, **DO3** was added to **P(VDF-TrFE)** 20% w/v solution in different % w/w with respect to the polymer content. The same cosolvent mixture of (4:6) volume ratio of DMF/acetone was used, and the polymer/dye solution was stirred at room temperature until a uniform and clear solution was obtained.

4.1.2. Films. Thin films were prepared by spin-coating the polymer/dye solutions using a spin coater (Laurell Technologies, model WS—400B—6NPP/lite) at 3000 rpm for 50 s.

4.1.3. Nanofiber Mats. Nanofiber mats were prepared by electrospinning using a horizontal electrospinning setup. The voltage was applied using a Spellman Sl-150 High Voltage Power Supply. The prepared solution (see above) was loaded into a 1 mL glass syringe (Hamilton Gastight, model 1002 TLL) with a stainless-steel needle (inner diameter = 22 gauge). The syringe was mounted on a mobile infusion pump (KDS Scientific, model series 200), which allowed us to set the flow rate. Nanofibers were randomly collected on a rectangular static collector, electrically grounded. Aligned nanofibers were deposited onto a cylindrical rotating collector. Samples were processed using the following parameters: needle-to-collector distance of 20 cm, applied voltage from 15 to 20 kV, and a solution flow rate of 0.05 mL h^{-1}.

4.2. Characterization. *4.2.1. FT-IR Spectroscopy.* The IR absorption spectra were recorded using a Thermo Nicolet NEXUS FT-IR spectrometer (4 cm^{-1} resolution, 128 scans) equipped with a Thermo Electron Corporation Continu*μ*m FT-IR Microscope. Dye powder samples were analyzed through a Diamond Anvil Cell (DAC) in transmission mode. Dye spectra in CCl$_4$ solution were recorded using a sealed cell type with a path length of 0.05 mm with KBr windows. Film spectra were recorded in transmission mode after depositing the solution on Si substrates. Spectra of nanofibers were recorded at room temperature in double reflection mode using reflecting aluminum substrates. For dichroism analysis of aligned nanofibers, a ZnSe wire grid IR polarizer was used with the same setup. For spectroscopic studies during thermal cycles on nanofiber samples, a Linkam heating cell (FT-IR 600) operating in a nitrogen atmosphere was used. In this case, the FT-IR analysis was carried out in transmission mode using the ZnSe window; nanofibrous mats previously deposited on aluminum foil during electrospinning were carefully cut with a lancet and transferred onto the ZnSe window.

4.2.2. Scanning Electron Microscopy and Energy-Dispersive Spectrometry. SEM images were taken by means of a Tescan scanning electron microscope (Tescan, MIRA3); for elemental analysis, a Zeiss scanning electron microscope (EVO 50 EP) equipped with an energy-dispersive spectrometer has been used. The accelerating voltages applied were ranging from 3 to 5 kV for imaging and from 15 to 20 kV for the elemental analysis. Fibers were directly deposited onto a silicon substrate, and no metallization was needed. The measurements of the nanofiber diameters were carried out by processing SEM images with the software ImageJ (Rasband, W.S., ImageJ, U.S. National Institutes of Health, Bethesda, Maryland, USA, http://imagej.nih.gov/ij/, 1997—2016). The statistical analysis of diameter distribution has been carried out with Origin software (ver. 2021) considering for each sample 100 independent measurements of fiber diameters.

4.2.3. Transmission Electron Microscopy. The microstructure of the nanofibers was examined by high-resolution TEM using a Philips CM200 field emission gun microscope. Fibers were deposited directly onto lacey carbon-coated copper grids and examined at an accelerating voltage of 200 kV.

4.3. Computational Methods. To investigate the behavior of **DO3** when blended with **P(VDF-TrFE)**, density functional theory (DFT)[21−24] calculations were performed on selected in vacuo molecular models with the Gaussian09 code[25] at the B3LYP/6-31G(d,p) level of theory,[26−29] a common choice for the calculation of equilibrium geometries, vibrational frequencies, and IR intensities of organic molecules. The D3 version of Grimme's dispersion with the Becke—Johnson damping was employed.[30] The choice of the 6-31G(d,p) basis set instead of more extended ones allowed us to study structures with several atoms within acceptable computational times. Geometry optimization of the molecular models was performed starting from guess geometries obtained through MMFF94, a Merck molecular force field, as implemented in the Open Babel Toolbox.[31,32] DFT vibrational normal mode frequencies and IR intensities were computed within the harmonic approximation.

■ ASSOCIATED CONTENT

ⓢ Supporting Information

The Supporting Information is available free of charge at https://pubs.acs.org/doi/10.1021/acsomega.2c00363.

SEM micrographs of **P(VDF-TrFE)**/**DO3** nanofibers and diameter distribution plots and sketches of the structures of **DO3**..**PVDF** interacting models after geometry optimization at the MMFF94 level (PDF)

■ AUTHOR INFORMATION

Corresponding Author

Chiara Castiglioni − *Dipartimento di Chimica, Materiali e Ingegneria Chimica Giulio Natta, Politecnico di Milano, 20133 Milano, Italy;* ⓞ orcid.org/0000-0002-6945-9157; Phone: +39 0223993230; Email: chiara.castiglioni@polimi.it

Authors

Alessia Arrigoni − *Dipartimento di Chimica, Materiali e Ingegneria Chimica Giulio Natta, Politecnico di Milano, 20133 Milano, Italy;* ⓞ orcid.org/0000-0001-9682-0043

Gianluca Serra − *Dipartimento di Chimica, Materiali e Ingegneria Chimica Giulio Natta, Politecnico di Milano, 20133 Milano, Italy*

Jacopo Manidi − *Dipartimento di Chimica, Materiali e Ingegneria Chimica Giulio Natta, Politecnico di Milano, 20133 Milano, Italy*

Chiara Bertarelli − *Dipartimento di Chimica, Materiali e Ingegneria Chimica Giulio Natta, Politecnico di Milano, 20133 Milano, Italy; Center for Nano Science and*

Technology@PoliMi, Istituto Italiano di Tecnologia, 20133 Milano, Italy

Notes
The authors declare no competing financial interest.

■ ACKNOWLEDGMENTS

■ ADDITIONAL NOTE

[1] The copolymer band at 1402 cm^{-1} is associated with the CH$_2$ wagging of the polymer chains; the B$_1$ symmetry of the associated phonons guarantees that this band has a dipole moment vector which is directed along the polymer chain axis. The parallel polarization behavior of this band in aligned nanofibers denotes that in this system, the polymer chains are mostly directed parallel to the fiber axis.[20]

■ REFERENCES

(1) Prasad, P. N.; Williams, D. J.; Wiley, J. *Introduction to Nonlinear Optical Effects in Molecules and Polymers*; A Wiley-Interscience Publication: 1991, vol. *320*.

(2) Williams, D. J. Nonlinear Optical Properties of Organic and Polymeric Materials. In *ACS synposium series*, 1983, vol. *233*.

(3) Chemla, D. S. *Nonlinear Optical Properties of Organic Molecules and Crystals V1*; Elsevier: 1987, p. 497.

(4) Marder, S. R.; Sohn, J. E.; Stucky, G. D. *Materials for Nonlinear Optics Chemical Perspectives*; American Chemical Society: Washington, DC, 1991; vol. *455*, p. 16.

(5) Samyn, C.; Verbiest, T.; Persoons, A. Second-Order Non-Linear Optical Polymers. *Macromol. Rapid Commun.* **2000**, *21*, 1−15.

(6) Burland, D. M.; Miller, R. D.; Walsh, C. A. Second-Order Nonlinearity in Poled-Polymer Systems. *Chem. Rev.* **1994**, *94*, 31−75.

(7) Burganov, T. I.; Katsyuba, S. A.; Vakhonina, T. A.; Sharipova, A. V.; Fominykh, O. D.; Balakina, M. Y. Supramolecular Organization of Solid Azobenzene Chromophore Disperse Orange 3, Its Chloroform Solutions, and PMMA-Based Films. *J. Phys. Chem. C* **2018**, *122*, 1779−1785.

(8) Yesodha, S. K.; Sadashiva Pillai, C. K.; Tsutsumi, N. Stable Polymeric Materials for Nonlinear Optics: A Review Based on Azobenzene Systems. *Prog. Polym. Sci.* **2004**, *29*, 45−74.

(9) Ghebremichael, F.; Kuzyk, M. G.; Lackritz, H. S. Nonlinear Optics and Polymer Physics. *Prog. Polym. Sci.* **1997**, *22*, 1147−1201.

(10) Shalin, N. I.; Fominykh, O. D.; Balakina, M. Y. Effect of Dimer Formation via Hydrogen Bonding on Static and Dynamic Nonlinear Optical Characteristics of Chromophores. *Int. J. Quantum Chem.* **2020**, *120*, No. e26061.

(11) Fominykh, O. D.; Sharipova, A. V.; Balakina, M. Y. Molecular Modeling of Methacrylic Composite Materials Doped with Nonlinear Optical Azochromophores with Various Acceptor Fragments. *Comput. Mater. Sci.* **2022**, *201*, No. 110909.

(12) Liu, Z.; Ma, J. Effects of External Electric Field and Self-Aggregations on Conformational Transition and Optical Properties of Azobenzene-Based D-π-A Type Chromophore in THF Solution. *J. Phys. Chem. A* **2011**, *115*, 10136−10145.

(13) Möncke, D.; Mountrichas, G.; Pispas, S.; Kamitsos, E. I. Orientation Phenomena in Chromophore DR1-Containing Polymer Films and Their Non-Linear Optical Response. *Mater. Sci. Eng., B* **2011**, *176*, 515−520.

(14) Priimagi, A.; Cattaneo, S.; Ras, R. H. A.; Valkama, S.; Ikkala, O.; Kauranen, M. Supramolecular Guest-Host Systems: Combining High Dye Doping Level with Low Aggregation Tendency. In *Linear*

Nonlinear Optics of Organic Materials VI; SPIE: 2006; vol. *6331*, pp. 174−182.

(15) Vasilyev, I. V.; Fominykh, O. D.; Balakina, M. Y. Dynamic First Hyperpolarizability of Trans- and Cis-Isomers of Azobenzene Chromophore DO3 Calculated at DFT and MP2 Levels. *Comput. Theor. Chem.* **2018**, *1139*, 1−8.

(16) Robin, P.; Chastaing, E.; Broussoux, D.; Raffy, J.; Pocholle, J. P. Optical Second Harmonic Generation in Copolymers P(VDF-TRFE). *Ferroelectrics* **1989**, *94*, 133−137.

(17) Ishigure, T.; Aruga, Y.; Koike, Y. High-Bandwidth PVDF-Clad GI POF with Ultra-Low Bending Loss. *J. Light. Technol.* **2007**, *25*, 335−345.

(18) Faiz, F.; Baxter, G.; Collins, S.; Sidiroglou, F.; Cran, M. Polyvinylidene Fluoride Coated Optical Fibre for Detecting Perfluorinated Chemicals. *Sens. Actuators, B* **2020**, *312*, No. 128006.

(19) Tsutsumi, N.; Fujii, I.; Ueda, Y.; Kiyotsukuri, T. Second Harmonic Generation from a NLO Dye Aligned by the Internal Electric Field in a Blend of Poly(Vinylidene Fluoride) and Poly(Methyl Methacrylate). *Macromolecules* **1995**, *28*, 950−955.

(20) Arrigoni, A.; Brambilla, L.; Bertarelli, C.; Serra, G.; Tommasini, M.; Castiglioni, C. P(VDF-TrFE) Nanofibers: Structure of the Ferroelectric and Paraelectric Phases through IR and Raman Spectroscopies. *RSC Adv.* **2020**, *10*, 37779−37796.

(21) Hohenberg, P.; Kohn, W. Inhomogeneous Electron Gas. *Phys. Rev.* **1964**, *136*, B864.

(22) Kohn, W.; Sham, L. J. Self-Consistent Equations Including Exchange and Correlation Effects. *Phys. Rev.* **1965**, *140*, A1133.

(23) Parr, R. G.; Weitao, Y. Density-Functional Theory of Atoms and Molecules. In *Horizons of Quantum Chemistry*; Springer: Dordrecht, 1995

(24) Salahub, D. R.; Zerner, M. C. The Challenge of d and f Electrons. In *Chemical Congress of North America 1988: Toronto, Ontario*; American Chemical Society, 1989; vol. *394*, p. 41.

(25) Frisch, M. J.; Trucks, G. W.; Schlegel, H. B.; Scuseria, G. E.; Robb, M. A.; Cheeseman, J. R.; Scalmani, G.; Barone, V.; Petersson, G. A.; Nakatsuji, H.; Li, X.; Caricato, M.; Marenich, A.; Bloino, J.; Janesko, B. G.; Gomperts, R.; Mennucci, B.; Hratchian, H. P.; Ortiz, J. V.; Izmaylov, A. F.; Sonnenberg, J. L.; Williams-Young, D.; Ding, F.; Lipparini, F.; Egidi, F.; Goings, J.; Peng, B.; Petrone, A.; Henderson, T.; Ranasinghe, D.; Zakrzewski, V. G.; Gao, J.; Rega, N.; Zheng, G.; Liang, W.; Hada, M.; Ehara, M.; Toyota, K.; Fukuda, R.; Hasegawa, J.; Ishida, M.; Nakajima, T.; Honda, Y.; Kitao, O.; Nakai, H.; Vreven, T.; Throssell, K.; Montgomery, J. A.; Peralta, J. J. E.; Ogliaro, F.; Bearpark, M.; Heyd, J. J.; Brothers, E.; Kudin, K. N.; Staroverov, V. N.; Keith, T.; Kobayashi, R.; Normand, J.; Raghavachari, K.; Rendell, A.; Burant, J. C.; Iyengar, S. S.; Tomasi, J.; Cossi, M.; Millam, J. M.; Klene, M.; Adamo, C.; Cammi, R.; Ochterski, J. W.; Martin, R. L.; Morokuma, K.; Farkas, O.; Foresman, J. B.; Fox, D. J. *Gaussian 09 (Revision D.01)*; Gaussian, Inc.: Wallingford, CT, 2016.

(26) Becke, A. D. Density-functional Thermochemistry. III. The Role of Exact Exchange. *J. Chem. Phys.* **1993**, *98*, 5648.

(27) Lee, C.; Yang, W.; Parr, R. G. Development of the Colle-Salvetti Correlation-Energy Formula into a Functional of the Electron Density. *Phys. Rev. B* **1988**, *37*, 785.

(28) Vosko, S. H.; Wilk, L.; Nusair, M. Accurate Spin-Dependent Electron Liquid Correlation Energies for Local Spin Density Calculations: A Critical Analysis. *Can. J. Phys.* **1980**, *58*, 1200−1211.

(29) Stephens, P. J.; Devlin, F. J.; Chabalowski, C. F.; Frisch, M. J. Ab Initio Calculation of Vibrational Absorption and Circular Dichroism Spectra Using Density Functional Force Fields. *J. Phys. Chem.* **1994**, *98*, 11623−11627.

(30) Grimme, S.; Ehrlich, S.; Goerigk, L. Effect of the Damping Function in Dispersion Corrected Density Functional Theory. *J. Comput. Chem.* **2011**, *32*, 1456−1465.

(31) Halgren, T. A. Merck Molecular Force Field. 11. MMFF94 van Der Waals and Electrostatic Parameters for Intermolecular Interactions. *J. Comput. Chem.* **1996**, *17*, 520−552.

(32) Halgren, T. A. Merck Molecular Force Field. I. Basis, Form, Scope, Parameterization, and Performance of MMFF94. *J. Comput. Chem.* **1996**, *17*, 490−519.

(33) Bianco, A.; Iardino, G.; Manuelli, A.; Bertarelli, C.; Zerbi, G. Strong Orientation of Polymer Chains and Small Photochromic Molecules in Polyamide 6 Electrospun Fibers. *ChemPhysChem* **2007**, *8*, 510−514.

(34) Yarin, A. L.; Kataphinan, W.; Reneker, D. H. Branching in Electrospinning of Nanofibers. *J. Appl. Phys.* **2005**, *98*, No. 064501.

(35) Reneker, D. H.; Yarin, A. L.; Fong, H.; Koombhongse, S. Bending Instability of Electrically Charged Liquid Jets of Polymer Solutions in Electrospinning. *J. Appl. Phys.* **2000**, *87*, 4531.

(36) Koombhongse, S.; Liu, W.; Reneker, D. H. Flat Polymer Ribbons and Other Shapes by Electrospinning. *J. Polym. Sci. B Polym. Phys.* **2001**, *39*, 2598−2606.

(37) Gevorkyan, A.; Shter, G. E.; Shmueli, Y.; Buk, A.; Meir, R.; Grader, G. S. Branching Effect and Morphology Control in Electrospun $PbZr_{0.52}Ti_{0.48}O_3$ Nanofibers. *J. Mater. Res.* **2014**, *29*, 1721−1729.

(38) Sohrabi, A.; Shaibani, P. M.; Thundat, T. The Effect of Applied Electric Field on the Diameter and Size Distribution of Electrospun Nylon6 Nanofibers. *Scanning* **2013**, *35*, 183−188.

(39) Li, T.; Feng, Z. Q.; Qu, M.; Yan, K.; Yuan, T.; Gao, B.; Wang, T.; Dong, W.; Zheng, J. Core/Shell Piezoelectric Nanofibers with Spatial Self-Orientated β-Phase Nanocrystals for Real-Time Micropressure Monitoring of Cardiovascular Walls. *ACS Nano* **2019**, *13*, 10062−10073.

(40) Li, T.; Qu, M.; Carlos, C.; Gu, L.; Jin, F.; Yuan, T.; Wu, X.; Xiao, J.; Wang, T.; Dong, W.; Wang, X.; Feng, Z. Q. High-Performance Poly(Vinylidene Difluoride)/Dopamine Core/Shell Piezoelectric Nanofiber and Its Application for Biomedical Sensors. *Adv. Mater.* **2020**, *33*, No. 2006093.

(41) Pimentel, G. C.; McClellan, A. L. *The Hydrogen Bond*; W.H. Freeman and Company; San Francisco and London, 1960.

(42) Galimberti, D.; Milani, A.; Castiglioni, C. Infrared Intensities and Charge Mobility in Hydrogen Bonded Complexes. *J. Chem. Phys.* **2013**, *139*, No. 074304.